WO₃–TiO₂ based catalysts for the simulated solar radiation assisted photocatalytic ozonation of emerging contaminants in a municipal wastewater treatment plant effluent

A. Rey [a],[*], P. García-Muñoz [a], M.D. Hernández-Alonso [b], E. Mena [a],
S. García-Rodríguez [c], F.J. Beltrán [a]

[a] Departamento de Ingeniería Química y Química Física, Universidad de Extremadura, Av. Elvas s/n, 06006 Badajoz, Spain
[b] División de Energía Renovable, CIEMAT, Av. Complutense 40, 28040 Madrid, Spain
[c] Instituto de Catálisis y Petroleoquímica, CSIC, Av. Marie Curie, 2, 28049 Madrid, Spain

ABSTRACT

This work is focused on the use of TiO_2–WO_3 photocatalysts for the removal of a mixture of emerging contaminants through photocatalytic ozonation using simulated solar light as radiation source. Own-made TiO_2–WO_3 catalysts with WO_3 content around 4 wt% were synthesized using P25 and titanate nanotubes as TiO_2 starting materials. Photocatalysts were thoroughly characterized by means of ICP–OES, N_2 adsorption–desorption isotherms, XRD, TEM, Raman, XPS and DR–UV–Vis spectroscopy. Photocatalytic ozonation using WO_3 based titanate nanotubes composite gave place to complete removal of emerging contaminants (caffeine, metoprolol and ibuprofen in a Municipal Wastewater Treatment Plant effluent aqueous matrix) in less than 40 min with TOC removal up to 64% after 2 h. The highest catalytic activity of this material in the reaction under study compared to bare TiO_2 is due to several effects such as higher activity under visible light radiation joined to an increase in adsorption capacity of organic compounds and catalytic ozonation ability caused by the presence of WO_3.

© 2014 Elsevier B.V. All rights reserved.

1. Introduction

Emerging contaminants (ECs), such as pharmaceuticals and personal care products, which usually present endocrine disrupting activity, are frequently detected in wastewater and aquatic environments [1,2]. These contaminants can cause severe adverse effects in human and wildlife and their removal is of a great concern on environmental and health risk management [2,3]. However these compounds are hardly biodegradable so they are not removed by conventional treatment at municipal wastewater treatment plants (MWWTPs), and therefore advanced treatment technologies are required [1].

Advanced oxidation processes (AOPs) which involve the formation of highly reactive species such as hydroxyl radical (HO•), have demonstrated their efficiency to degrade many ECs transforming them into harmless products [4]. Among these AOPs, photocatalytic ozonation, i.e., the combination of photocatalytic oxidation and ozone processes, can greatly enhance the rates of ECs degradation and, specially, the mineralization achieved by the single processes [5–7]. In fact, a synergistic effect has been observed between ozone and irradiated photocatalyst due to both the strong electron trapping effect of ozone, that avoids, to some extent, the electron–hole recombination process, and to the reaction of ozone with the superoxide ion radical ($O_2^{•-}$, intermediate species in photocatalytic reactions). In these two steps the ozonide ion radical ($O_3^{•-}$) is generated and further transformed into HO•, thus increasing the concentration of this highly reactive species in the aqueous medium [5,8,9].

One of the most important aspects in the application of photocatalytic wastewater treatment technologies is the cost derived from the radiation source operation and maintenance. The use of solar energy as radiation source avoids this drawback leading to more economic technologies [10]. However, most of the photocatalytic ozonation studies conducted to date make use of TiO_2 as photocatalyst that only uses around 5% of solar radiation (UV range). Different methods to solve this limitation, mainly applied to ozone-free photocatalytic oxidation processes, have been developed, such as ion doping, modification of TiO_2 surface with noble metals, metal ion implantation or coupling semiconductors [10,11].

In this line, composite materials of coupled WO_3 and TiO_2 semiconductors can extend the absorption of radiation to the visible region as a result of the lower band gap energy of WO_3 (around 2.7 eV), and also allow a wide electron–hole separation avoiding recombination to some extent [11]. TiO_2–WO_3 coupled semiconductors have been successfully applied to the degradation of different organic contaminants in water through photocatalytic oxidation under visible light radiation [12–16]. In addition, these materials combined with gold nanoparticles have also been tested for photocatalytic ozonation of model compounds such as oxalic acid and TNT giving place to promising results [17,18].

This work has been focused on the use of different TiO_2–WO_3 composite catalysts to extend the radiation absorption to visible light and make better use of the solar emission spectrum in photocatalytic ozonation process applied to wastewater detoxification. Two different TiO_2 supports, commercial TiO_2 P25 and own-made titanate nanotubes, which present very different textural and structural properties, have been used. The synthesized materials were tested in photocatalytic ozonation of ibuprofen (IBP), metoprolol (MTP) and caffeine (CAF) in a spiked municipal wastewater effluent from a secondary treatment and using simulated solar light as radiation. These contaminants, IBP, a nonsteroidal anti-inflammatory drug for pain relief and fever reduction; MTP, a β-blocker used for several cardiovascular diseases; and CAF, a stimulant drug mainly from coffee consumption, have been selected because of their frequent presence in municipal wastewater [2].

2. Experimental

2.1. Catalysts preparation

Aeroxide TiO_2 P25 (anatase/rutile 80/20, 21 nm crystal size) was used as the starting photocatalytic material. The procedure to obtain titanate nanotubes catalyst (NT) has been reported in previous works [19,20]. Briefly, 1 g of the precursor P25 was hydrothermally treated at 130 °C in 70 mL of 10 M NaOH in a Teflon-lined autoclave, during 48 h. The mixture was stirred for 30 min before and after the thermal treatment. In a second stage, the obtained powders were thoroughly washed using diluted HCl. The powders were recovered from the solutions by centrifugation, dried at 100 °C overnight and then calcined in air atmosphere for 3 h at 350 °C.

P25 and NT photocatalysts were coated with nanosized WO_3 particles (P25–WO_3 and NT–WO_3 samples) as described elsewhere [18]. First 0.216 g H_2WO_4 were added in 100 mL of ultrapure water and then aqueous ammonia solution was added drop wise until the tungstic acid was completely dissolved. Further 5 g of P25 or NT were added under continuous stirring and the obtained mixture was stirred for 30 min and then acidified to pH 4 with 0.5 M HCl. Then 10 mL of an aqueous solution of oxalic acid 0.1 M was added to the mixture and stirred for 1 h at 40 °C to prevent the aggregation of WO_X particles in the precipitate. Finally the solid was recovered by filtration, dried at 110 °C for 2 h and then calcined in air atmosphere for 2 h at 420 °C. The TiO_2–WO_3 thus prepared had a theoretical amount of WO_3 of 3.8 wt%. For comparative purposes, NT photocatalyst was also calcined in air atmosphere for 2 h at 420 °C (sample NT–T).

2.2. Characterization

Total tungsten content of the catalysts was analyzed by inductively coupled plasma with an ICP–OES Optima 3300DV (Perkin-Elmer) after acidic microwave digestion of the samples.

BET surface area and pore volume of the photocatalysts were determined from their nitrogen adsorption–desorption isotherms obtained at −196 °C using an Autosorb 1 apparatus (Quantachrome). Prior to analysis the samples were outgassed at 250 °C for 12 h under high vacuum (<10^{-4} Pa).

The crystalline phases present in the photocatalysts were inferred from their X-ray diffraction (XRD) patterns recorded using a powder Bruker D8 Advance XRD diffractometer with a Cu $K\alpha$ radiation (λ = 0.1541 nm). The data were collected from 2θ = 20° to 80° at a scan rate of 0.02 s^{-1} and 1 s per point.

A JEM-2100F 200 kV transmission electron microscope (JEOL Ltd.) and a TEM Tecnai G20 Twin 200 kV transmission electron microscope (FEI Company) were used to study the crystallinity and morphology of the samples.

Raman spectra were obtained using a Nicolet Almega XR Dispersive micro-Raman (Thermo Scientific) with a spectral resolution of 2 cm^{-1}. The samples were excited at 633 nm with the laser beam power at 100% and 200 scans accumulation.

X-ray photoelectron spectra (XPS) were obtained with a $K\alpha$ Thermo Scientific apparatus with an Al $K\alpha$ ($h\nu$ = 1486.68 eV) X-ray source using a voltage of 12 kV under vacuum (2×10^{-7} mbar). Binding energies were calibrated relative to the C1s peak from carbon samples at 284.6 eV. The resulting XPS peaks were curve-fitted to a combination of Gaussian and Lorentzian functions using a Shirley type background for peak analysis.

Diffuse reflectance UV–Vis spectroscopy (DR-UV–Vis) measurements, useful for the determination of the semiconductor band gap, were performed with an UV–Vis–NIR Cary 5000 spectrophotometer (Varian-Agilent Technologies) equipped with an integrating sphere device.

2.3. Catalytic activity measurements

Ibuprofen sodium salt (IBP), metoprolol tartrate (MTP) and caffeine (CAF) were used as target contaminants to test the catalytic activity of the synthesized materials. They were added to a real municipal wastewater effluent (MWW) taken from Badajoz MWWTP (Badajoz, Spain) designed for 225,000 inhabitants with an average inlet flow of 37,500 m^3 day^{-1}. Effluents were collected downstream of the MWWTP secondary biological treatment, filtered and stored at −20 °C until use.

Photocatalytic experiments were carried out in semi-batch mode in a laboratory-scale system consisting of a 0.5 L glass-made spherical reactor, provided with a gas inlet, a gas outlet and a liquid sampling port. The reactor was placed in the chamber of a commercial solar simulator (Suntest CPS, Atlas) provided with a 1500 W air-cooled Xe arc lamp with emission restricted to wavelengths over 320 nm because of the presence of quartz, glass and polyester cut-off filters. The irradiation intensity was kept at 550 W m^{-2} and the temperature of the system was maintained between 25 and 35 °C throughout the experiments. If required, a laboratory ozone generator (Anseros Ozomat Com AD-02) was used to produce a gaseous ozone–oxygen stream that was fed to the reactor. In that case, the ozone concentration was recorded on an Anseros Ozomat GM-6000Pro gas analyzer. A scheme of the experimental set-up is depicted in Fig. 1.

In a typical photocatalytic ozonation experiment, the reactor was first loaded with 0.5 L of an aqueous solution containing 2 mg L^{-1} of ECs initial concentration in the MWW effluent. Then, 0.25 g of the catalyst were added and the suspension was stirred in the darkness for 30 min while bubbling air to the system. After this dark stage, the lamp was switched on and, simultaneously, a mixture of ozone–oxygen (10 mg L^{-1} ozone concentration) was fed to the reactor at a flow rate of 20 L h^{-1}. The irradiation time for each experiment was 2 h. Samples were withdrawn from the reactor at intervals and filtered through a 0.2 μm PET membrane to remove the photocatalyst particles.
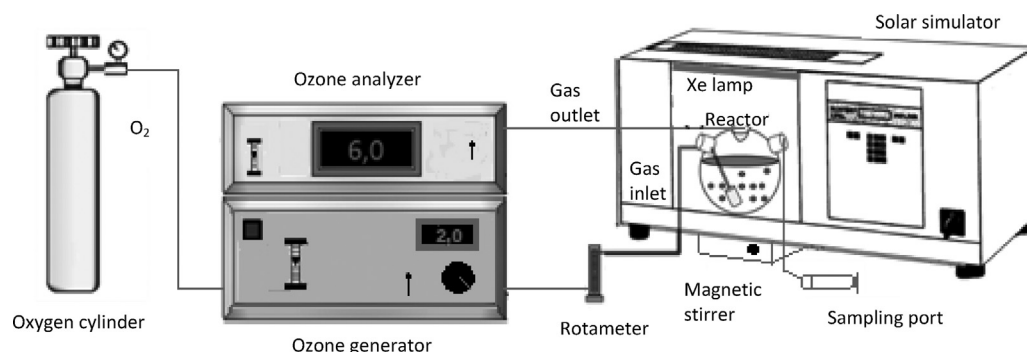
Fig. 1. Scheme of the experimental set-up.

Experiments of adsorption (i.e., absence of radiation and ozone), photolysis (i.e., radiation in absence of catalysts and ozone), photocatalytic oxidation (i.e., radiation and catalyst in absence of ozone), ozonation (i.e., absence of radiation and catalyst), catalytic ozonation (i.e., absence of radiation) were also carried out for comparative analysis. In addition, photocatalytic oxidation experiments of IBP were carried out under visible radiation using a polyester wavelength cut-off filter below 390 nm.

ECs concentrations were analyzed by high-performance liquid chromatography HPLC-DAD (Hitachi, Elite LaChrom) using a Phenomenex C-18 column (5 μm, 150 mm long, 3 mm diameter) as stationary phase and 0.5 mL min^{-1} of acetonitrile-acidified water (0.1% H_3PO_4) as mobile phase (from 5% to 60% in acetonitrile) during 25 min and 10 min re-equilibration time). Identification and quantification was carried out at 220 nm. Total organic carbon (TOC) and inorganic carbon (IC) were measured using a Shimadzu TOC-V$_{SCH}$ analyzer. Aqueous ozone concentration was measured by following the indigo method using an UV–Vis spectrophotometer (Evolution 201, Thermospectronic) set at 600 nm [21]. Ozone concentration in the gas phase was continuously monitored by means of an Anseros Ozomat GM-6000Pro analyzer. Finally, chemical oxygen demand (COD) was determined by means of the dichromate method, using Dr. Lange cuvette test; biological oxygen demand (BOD$_5$) was analyzed by a respirometric method using an Oxitop® WTW system; aromaticity as the absorbance of the sample at 254 nm and phosphates by means of colorimetric method using a Merck Spectroquant kit (UV–Vis spectrophotometry, Evolution 201 from Thermospectronic).

3. Results and discussion

3.1. Characterization of the photocatalysts

Table 1 summarizes tungsten content, some textural parameters, band gap energy and absorption edge wavelength of the photocatalysts. It can be seen that the W mass composition (expressed as WO_3) of the TiO_2–WO_3 catalysts was close but somewhat higher to the nominal value expected (3.8 wt%).

Fig. 2 shows N_2 adsorption–desorption isotherms where it can be noticed that P25 based catalysts are non-porous materials with type II isotherms whereas NT catalysts presented type IV isotherms with H3 hysteresis loops characteristics of mesoporous solids, according to IUPAC classifications [22]. On the other hand, the incorporation of W did not change the isotherm aspect of these photocatalysts respect their supports. Main differences are observed for NT catalysts where the incorporation of W procedure has changed the slope and shifted the hysteresis loop in NT–WO_3 respect to NT, indicating a lower porosity. This is mainly related to the heat-treatment applied, as can be deduced from the similarity of the isotherms of NT–T and NT–WO_3. Calcination at 420 °C triggers

structural changes as discussed below [20]. From these analyses, specific surface area (S_{BET}) and pore volume (V_{PORE}) were calculated (see Table 1). As can be observed P25 based catalysts show S_{BET} values according to that indicated by the supplier for P25 (around 50 m^2 g^{-1}), and similar pore volume around 0.25 m^3 g^{-1}. Thus, the incorporation of W and calcination of the composite material does not significantly affect its textural properties. On the other hand, NT presented higher S_{BET} and pore volume, according to its mesoporous structure as it was previously reported for similar materials [20]. In this case, the incorporation of W has favoured a decrease in the surface area and pore volume of the NT–WO_3 catalyst mainly due to the calcination step, although some pore blockage after W deposition cannot be disregarded according to the lower values of textural parameters of this catalyst respect to the NT–T sample.

Structural characterization of the photocatalysts was accomplished by means of XRD, TEM and Raman analyses and results are depicted in Figs. 3–5, respectively. P25 based catalysts gave place to similar XRD patterns with main diffraction peaks attributable to anatase and rutile TiO_2 phases. The absence of peaks attributable to W species could be due to the low content in the catalysts and/or to the high dispersion of W. This was also confirmed, as Fig. 4 shows, by TEM micrographs where W particles were undistinguishable. In addition, heat-treatment applied to P25–WO_3 photocatalyst does not produce any significant change in the TiO_2 structure. Regarding NT photocatalyst, a shifted diffraction peak position at 24.9° respect to 25.4° for anatase is observed, indicating titanate structure [20]. TEM micrograph confirmed nanotubular morphology for NT sample (Fig. 4). On the other hand, the incorporation of W in NT–WO_3 photocatalyst led to a transformation of the titanate structure into anatase as evidenced by the shift of the corresponding diffraction
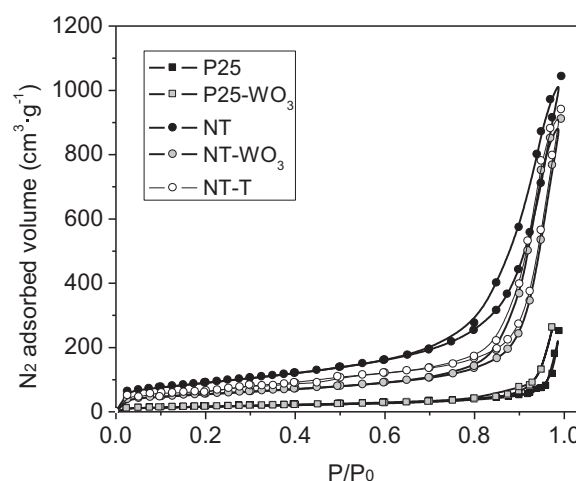

Fig. 2. N_2 adsorption–desorption isotherms of the catalysts.

Table 1
Properties of the catalysts.

Catalyst	WO_3 (wt%)	S_{BET} (m^2 g^{-1})	V_{PORE} (cm^3 g^{-1})	W_{XPS} (at%)	E_g (eV)	λ (nm)
P25	–	52	0.25	–	3.19	389
P25–WO$_3$	4.1	49	0.28	1.6	3.05	407
NT	–	320	1.39	–	3.18	390
NT–WO$_3$	4.5	195	1.17	0.9	2.98	416
NT–T	–	208	1.19	–	–	–

peaks (e.g., most intense from 24.9° to 25.3°) join to an increase in their intensity. This transformation is mainly related to the calcination step at 420 °C as the XRD pattern and TEM micrograph of the NT–T sample subjected to the same heat-treatment confirmed, and also according to results reported elsewhere [20]. TEM micrographs corroborated the transformation of titanate nanotubular structures to elongated anatase particles (Fig. 4). Fig. 5 shows Raman spectra of TiO$_2$–WO$_3$ photocatalysts. In Fig. 5(a) vibration peaks at 395, 517 and 638 cm^{-1} were observed in both catalysts (P25–WO$_3$ and NT–WO$_3$) which are unambiguously attributed to anatase phase of TiO$_2$ [23,24]. On the other hand, only for P25 based material, rutile phase is observed as a broad peak at 448 cm^{-1} according to the P25 structural composition [23,24]. These results also confirmed the transformation of titanate structure into anatase after calcination step [20]. The lowest intensity observed in the Raman spectra for the anatase vibrations can be related to the lowest crystallinity of NT–WO$_3$ photocatalyst according to XRD results [23]. On the other hand, Fig. 5(b) shows main W contributions to the Raman spectra. The band located around 792 cm^{-1} corresponds to weak second-order feature of anatase assigned to the first overtone band at 395 cm^{-1} [25]. At around 954 cm^{-1} appears another contribution assigned to the stretching mode of the terminal W=O bond which is characteristic of two-dimensional tungsten oxide surface species WO$_X$ [25,26]. In addition, the weak band located at around 1042 cm^{-1} could be related to the presence of WO$_X$ species in tetrahedral coordination [27]. The observed contributions at 954 and 1042 cm^{-1} together with the absence of any signal close to 800 cm^{-1} suggest that nothing of the added W contributes to

the formation of crystalline WO$_3$ [27]. These results are in a good agreement with XRD and TEM observations. Again it is noteworthy the lowest intensity of the NT–WO$_3$ spectrum as commented above.

Surface chemical composition of the catalysts was analyzed by XPS. Full spectra are depicted in Fig. 6(a)–(d) and confirmed the presence of O, Ti and C in all the samples (O 1s, Ti 2p and C 1s peaks). In addition, the peaks of W 4d and W 4f spectral regions appear in the full spectra of the TiO$_2$–WO$_3$ photocatalysts confirming the presence of W in their surfaces. No N signal was detected confirming the absence of N-doping effect due to the NH$_3$ used for the incorporation of W in composite catalysts. The surface content of W was calculated from peak areas and Wagner atomic sensitive factors [28]. Results are summarized in Table 1 where it can be noticed a lower W surface content for the NT–WO$_3$ catalyst that could be related to the higher porosity of the NT sample which can favour the incorporation of W in inner regions of the porous structure. On the other hand, Fig. 6(e) shows the high-resolution Ti 2p spectral region of P25–WO$_3$ catalyst as an example. The binding energy of the Ti 2p$_{1/2}$ and Ti 2p$_{3/2}$ core levels at 464.7 eV and 459.0 eV, respectively, together with their separation of 5.7 eV confirm the valence state of Ti as Ti^{4+} in TiO$_2$ [29,30]. Fig. 6(f) displays the high-resolution and peak-fitting results of W 4f and Ti 3p XPS spectra of P25–WO$_3$ catalyst as an example. Analysis of the W 4f region is complicated due to the interference from the Ti 3p level of the TiO$_2$. However, the position of the Ti 3p peak can be fixed and its area calculated from the Ti 2p peaks areas [28]. This makes possible to distinguish between the two signals (Ti 3p and W 4f) by deconvolution procedure, and to determine the valence of W from the position of the W 4f level. The binding energy of the peaks located at 37.8 eV and 35.7 eV corresponds to W 4f$_{5/2}$ and W 4f$_{7/2}$ components, respectively, and their area ratio of 3:4 confirm the presence of W as W^{6+} in WO$_3$ [18,30]. Similar results were obtained for NT–WO$_3$ catalyst (not shown).

The UV–Vis diffuse reflectance spectra of the photocatalysts (Fig. 7) showed a higher optical absorbance in the visible region above ca. 400 nm for TiO$_2$–WO$_3$ catalysts due to the WO$_3$ loading. The optical energy band gap (E_g) was calculated by means of Tauc's expression and results are summarized in Table 1 together with the wavelength of absorption edge. These values are approximate due to the need of extrapolation of the resulting curve (not shown). However a value of 3.19 eV was calculated for P25 catalyst similar to 3.2 eV previously reported for bare TiO$_2$ [11]. It is noticeable a decrease of band gap energy by coupling the TiO$_2$ with WO$_3$ from ca. 3.2 eV to 3.05 eV and 2.98 eV calculated for P25–WO$_3$ and NT–WO$_3$ catalysts, respectively, which is in agreement to previously reported values for similar materials [15]. These results indicate that both P25–WO$_3$ and NT–WO$_3$ can be promising photocatalysts to use visible light.

3.2. Visible light response of the photocatalysts

The effectiveness of the catalysts in the use of visible light was tested using IBP as target compound by cutting off all the wavelengths lower than 390 nm of the Xe lamp in the solar simulator. Results of photocatalytic depletion of IBP and its mineralization with all the catalysts synthesized are presented in Fig. 8.
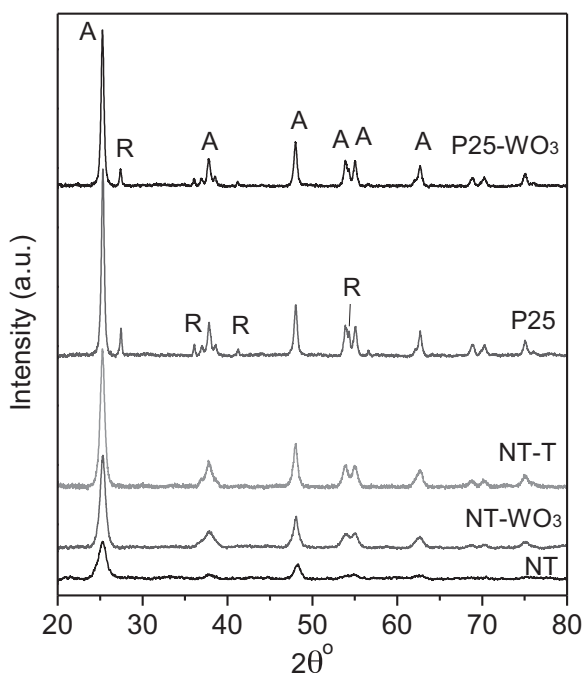

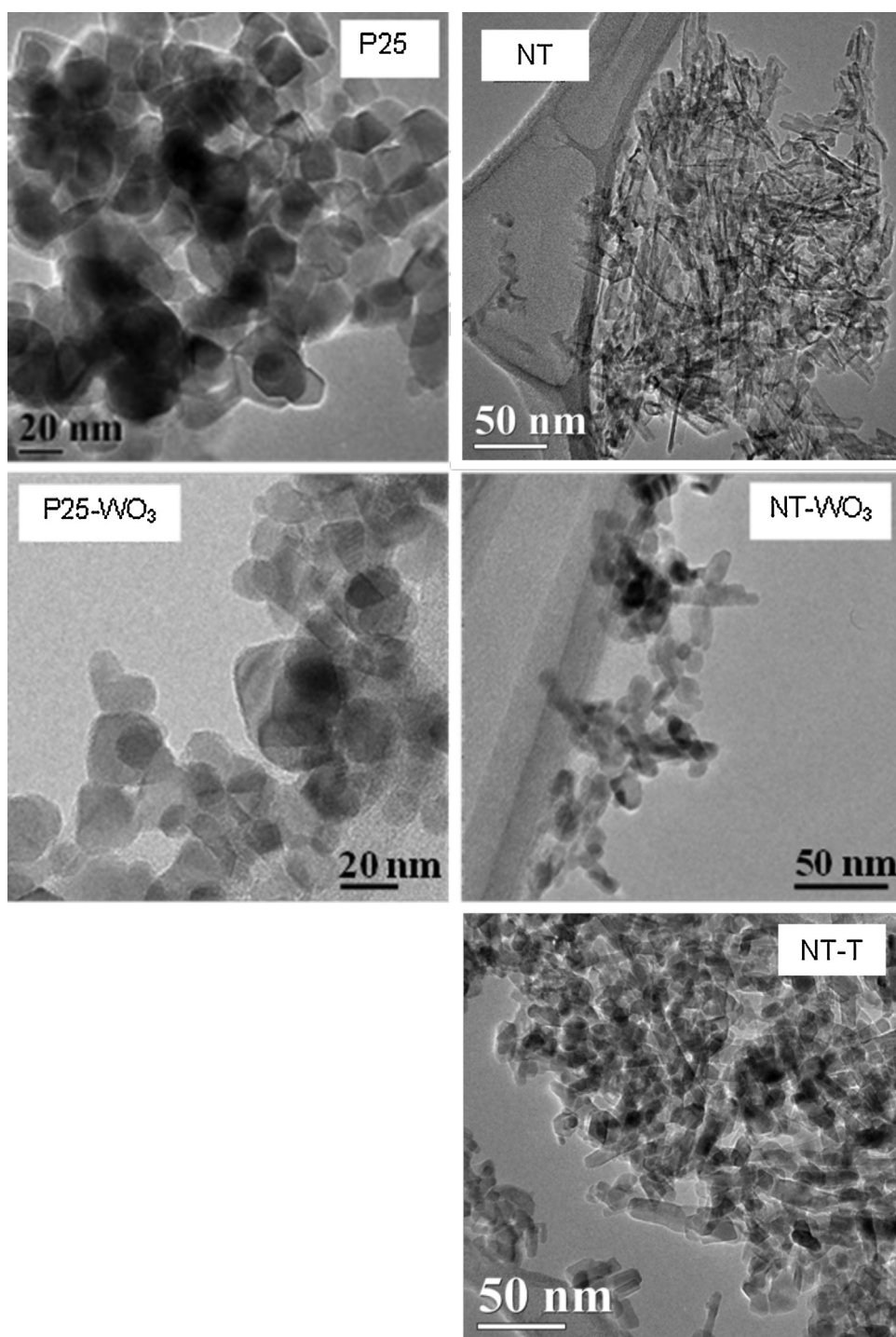**Fig. 3.** XRD patterns of the catalysts. Crystalline phases detected: anatase (A), rutile (R).

Fig. 4. TEM images of the catalysts.

Table 2
Characterization of MWW effluent before and after some treatments with NT–WO$_3$ catalyst ($t = 120$ min).

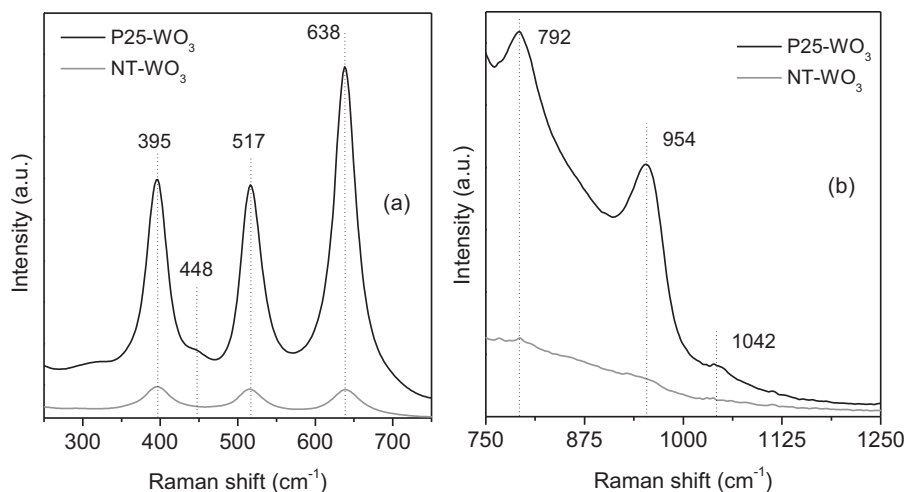| Parameter	Before treatment[*]	Photocatalytic oxidation	Ozonation	Catalytic ozonation	Photocatalytic ozonation
TOC (mgC L^{-1})	35.3	22.8	26.9	20.2	12.8
IC (mgC L^{-1})	42.0	40.1	38.3	41.5	36.4
pH	8.31	8.34	8.29	8.28	8.33
Absorbance 254 nm	0.253	0.164	0.116	0.058	0.017
COD (mgO$_2$ L^{-1})	51	46	41	33	17
BOD$_5$ (mgO$_2$ L^{-1})	32	-	-	-	-
Phosphate (mg L^{-1})	4	-	-	-	-

[*] Average values between all batches.

Fig. 5. Raman spectra of P25–WO$_3$ and NT–WO$_3$ photocatalysts.

Regarding IBP depletion (Fig. 8(a)), once confirmed the absence of IBP degradation through direct photolysis as expected according to its absorption UV–Vis spectrum, it can be noticed the positive effect of WO$_3$ loading on the photocatalytic activity of TiO$_2$–WO$_3$ photocatalysts under visible light irradiation compared to bare TiO$_2$. In addition, it is noticeable the lowest IBP degradation rate with the sample NT–T, thus indicating that the heat-treatment and different structural properties of the calcined NT are not responsible of the high catalytic activity in the NT–WO$_3$ photocatalyst. Also once the N-doping effect has been ruled out, the enhancement observed in the photocatalytic activity of the WO$_3$ coupled materials can be related to the lowest band gap energy observed (Table 1) due to WO$_3$ presence, which makes them easily excited by the visible light [15]. In addition, the presence of WO$_3$ can promote the charge transfer between photogenerated electrons from the conduction band of TiO$_2$ to the WO$_3$ conduction band, accompanied by holes transfer from the valence band of WO$_3$ to the TiO$_2$ valence band. The charge separation mechanism has been previously reported [15,17,18,27], and provokes an increase in the lifetime of the photogenerated pair electron/hole avoiding its recombination to some extent. As a consequence of both, higher visible light absorption and lower recombination rate, the photonic efficiency (i.e., reacted molecules/incident photons) of the photocatalytic process is increased. The improvement of composite materials respect their corresponding TiO$_2$ was higher in NT–WO$_3$ photocatalyst than P25–WO$_3$. Taking into account that NT–T sample led to a lower degradation rate than NT, the formation

of elongated anatase particles from the titanate structures seems not to be the reason of this behaviour. Thus, it seems plausible that NT material presented a better distribution and higher dispersion of WO$_3$ particles since also offered a developed porous structure and higher surface area than P25 together with a large ion-exchange capacity [19,20]. This hypothetic higher dispersion together with the slightly higher amount of WO$_3$ in NT–WO$_3$ (Table 1) could be the reasons of the higher visible light absorption capacity involving the largest improvement in NT–WO$_3$ photocatalytic activity compared to P25–WO$_3$, although additional characterization analysis confirming this hypothesis would be needed.

Regarding TOC evolution (Fig. 8(b)) it is noticeable the fastest mineralization rate observed with the NT–WO$_3$ photocatalyst reaching 40% TOC removal in 2 h whereas P25–WO$_3$ did not show a significant mineralization degree. These and previous results point out the higher photocatalytic activity of NT–WO$_3$ photocatalyst under visible light radiation.

3.3. Photocatalytic degradation of ECs in MWW

The effectiveness of the photocatalysts in a more realistic application was studied using a MWW effluent as aqueous matrix spiked with IBP, MTP and CAF. The average values of the main MWW secondary effluent parameters are summarized in Table 2. It can be highlighted the amount of carbonate/bicarbonate as inorganic carbon (IC) that was not removed prior to use and their buffer role maintaining the pH of the reaction medium around pH = 8.3.

Table 3
ECs removal (%) after 120 min reaction upon the different treatments applied.

Treatment	EC	No. catalyst			
Photolysis	IBP	0			
	CAF	5			
	MTP	7			

Treatment	EC	P25	P25–WO$_3$	NT	NT–WO$_3$
Adsorption	IBP	7	8	10	7
	CAF	8	7	4	6
	MTP	6	8	8	6
Photocatalysis	IBP	73	76	28	70
	CAF	77	79	31	82
	MTP	92	90	61	91

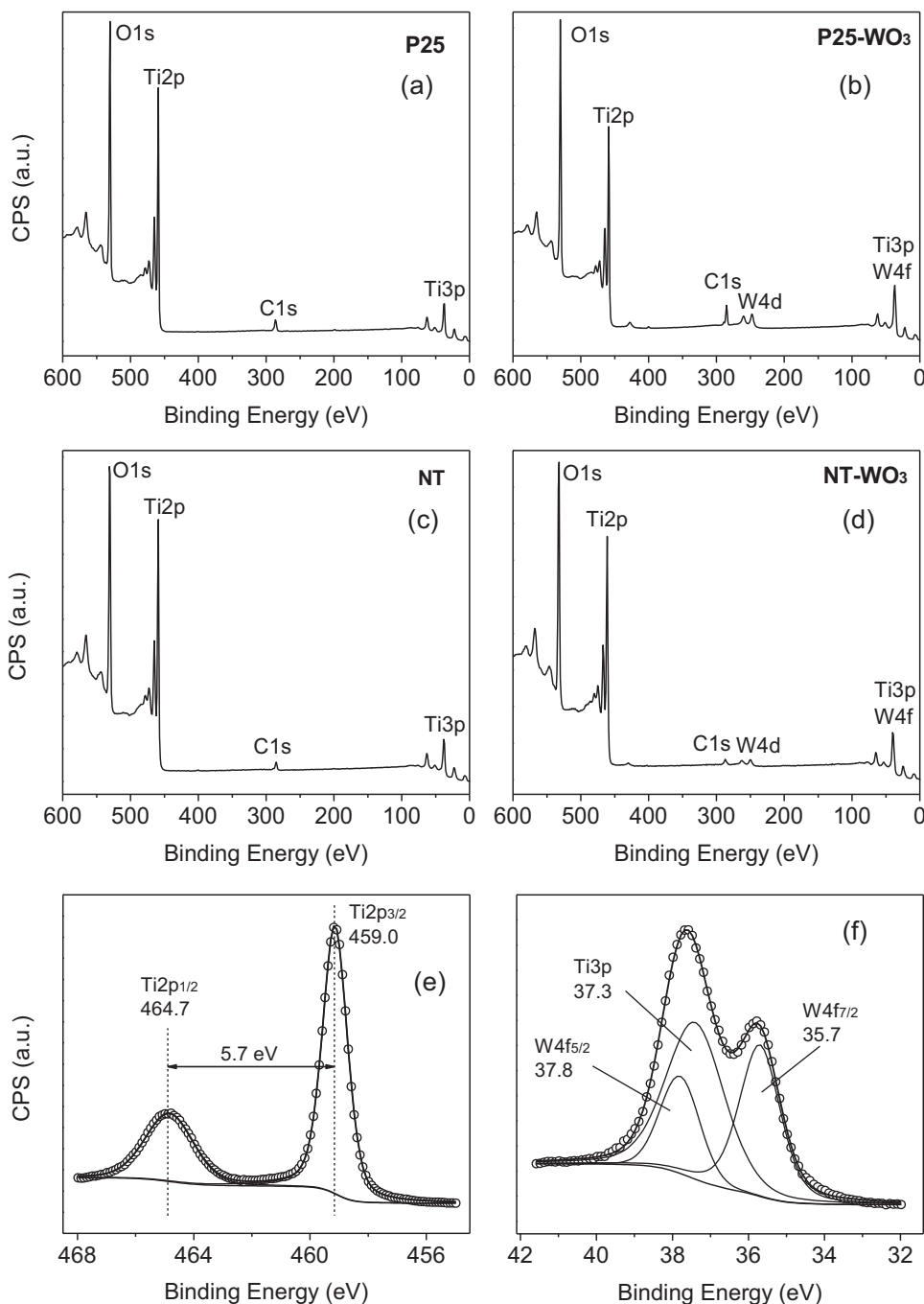| Treatment	EC	No. catalysts/all catalysts			
Ozonation	IBP				
Catalytic ozonation	CAF	>99.9			
Photocatalytic ozonation	MTP				

Fig. 6. XPS full spectra of the catalysts (a–d). High-resolution XPS spectra of Ti 2p (e) and Ti 3p/W 4f (f) spectral regions of P25–WO$_3$ catalyst.

Regarding the process applied, Table 3 summarizes the main results of ECs removal at 120 min upon the treatments tested, together with Figs. 9 and 10 that show the time-evolution of ECs and TOC, respectively, only for NT–WO$_3$ catalyst as an example. It can be noticed that direct photolysis exerts no effect on the case of IBP removal and only 5% and 7% removal was observed for CAF and MTP, respectively. The time-evolution of ECs concentration during photolysis is also shown in Fig. 9. Although these compounds do not absorb radiation in the wavelength range used in this work, MWW content could provoke indirect photolysis reactions [31,32]. The insignificant evolution of mineralization during photolysis can be observed in Fig. 10 and the low value of final TOC removal is also presented in Table 4. Taking into account that the contribution of the initial concentration of ECs to the initial TOC content

Table 4
TOC removal (%) after 120 min reaction upon the different treatments applied.

Treatment	No. catalysts			
Photolysis	4			
Ozonation	31			

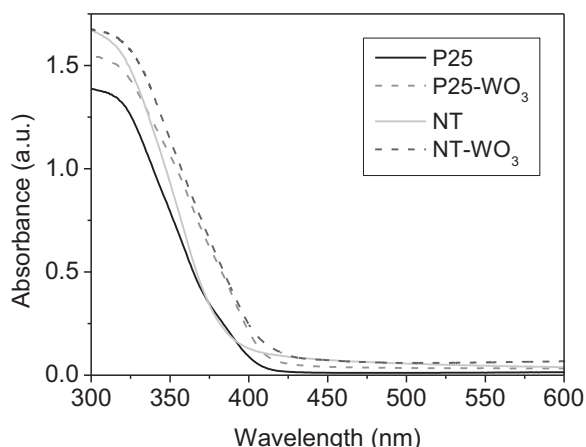| Treatment	P25	P25–WO$_3$	NT	NT–WO$_3$
Adsorption	3	17	9	23
Photocatalysis	37	42	31	37
Catalytic ozonation	23	48	39	47
Photocatalytic ozonation	47	55	42	64

Fig. 7. DR UV–Vis spectra of the catalysts.

is around 10% (3.7 mg L^{-1}), the mineralization observed would be mainly associated to the MWW TOC content.

Regarding the adsorption capacity of the catalysts, none of them gave place to ECs removal higher than 10% (Table 3). It is noticeable that no significant changes are observed in terms of ECs adsorption either due to W incorporation or textural properties modification in NT series, although the modification of adsorption capacity of these materials has been reported elsewhere [18]. However, a different behaviour is observed for the organic matter content of the MWW as the adsorption capacity of the catalysts is increased around 15% in both series, P25 and NT, after W incorporation (see values in Table 4). Also it is noticeable a somewhat higher adsorption capacity in NT series respect to P25 due to its more developed porous structure. The fact that NT series, in which a significant decrease in textural parameters was observed after calcination, presented the same increase in adsorption capacity than P25 series points out that this phenomenon is mainly related to the W species in the catalysts surface. In fact, it has been reported that the presence of a monolayer of WO$_X$ species on TiO$_2$ can significantly increase the surface acidity leading to the fact that composite materials TiO$_2$–WO$_3$ can adsorb more organic reactants [18,13].

For photocatalytic oxidation process with P25 series, as shown in Table 3, the incorporation of W did not give place to higher ECs removal, leading around 75%, 80% and 90% for IBP, CAF and MTP, respectively, with both P25 and P25–WO$_3$ catalysts. In spite of the improvement observed by introducing W when irradiated with visible light, bare P25 presents a higher catalytic activity under UVA

radiation and thus, when used the entire simulated solar light spectrum (320–800 nm), the beneficial effect of W is not noticeable. Similar results were observed in terms of mineralization (evolution not shown, final value given in Table 4). On the contrary, NT photocatalyst showed the poorest behaviour during the reaction but a significant increase in the photocatalytic activity of NT–WO$_3$ respect to NT precursor was noticed. Thus, in this case, ECs conversions around 70%, 80% and 90% for IBP, CAF and MTP, respectively, similar to those reached in P25 series were achieved. In addition, the order of reactivity during photocatalytic oxidation regardless of the catalyst used was MTP > CAF > IBP in contrast to the rate constants of the direct reaction of these ECs and hydroxyl radicals, HO$^\bullet$, (k_{OH-IBP} = 7.4 × 10^9 M^{-1} s^{-1} [33], k_{OH-CAF} = 5.9 × 10^9 M^{-1} s^{-1} [34], k_{OH-MTP} = 2.1 × 10^9 M^{-1} s^{-1} [35]). This may be an indication that not only HO$^\bullet$ attack is responsible of ECs removal but also different ways such as direct h$^+$ oxidation can be taking place.

All the ozone treatments led to complete ECs depletion in less than 45 min of reaction time (conversion higher than 99.9%) regardless of the presence/absence of catalysts and/or radiation in contrast to photocatalytic oxidation. Both direct and indirect ozone reactions may take place according to the pH = 8.3 of the reaction medium that was kept constant throughout the reaction time due to the buffer character of the MWW. On the other hand, slight differences can be noticed among ozone processes with a different behaviour mainly depending on the rate constant of the direct ozone-EC reaction (k_{O_3-IBP} = 9.1 M^{-1} s^{-1} [36], k_{O_3-CAF} = 6.5 × 10^2 M^{-1} s^{-1} [34], k_{O_3-MTP} = 6.2 × 10^3 M^{-1} s^{-1} (pH = 8) [37]). Although photocatalytic ozonation gave place to a faster depletion rate, it is noticeable in Fig. 9 that the differences between ozone processes are only significant for IBP which presented the lowest rate constant of direct ozone reaction, being practically negligible in the case of CAF and MTP. Main differences between ozone and O$_3$-catalytic processes were obtained in terms of TOC removal as shown in Table 4 and Fig. 10. Ozone alone led to 31% mineralization produced mainly during the first minutes of reaction time and then stopped likely due to the formation of refractory compounds to ozone attack. Production of HO$^\bullet$, main responsible species for mineralization, seems to be insufficient at pH = 8.3 in the ozonation process. The degree of mineralization is decreased in the presence of P25. This material does not have any positive effect in catalytic ozonation leading to even lower mineralization than ozone alone probably due to an inefficient consumption of O$_3$ onto the catalyst surface. In contrast, NT slightly increased TOC removal up to 39% that can be associated to the higher adsorption capacity of this material since mineralization rate is similar to ozone process (not shown). On the other hand, W
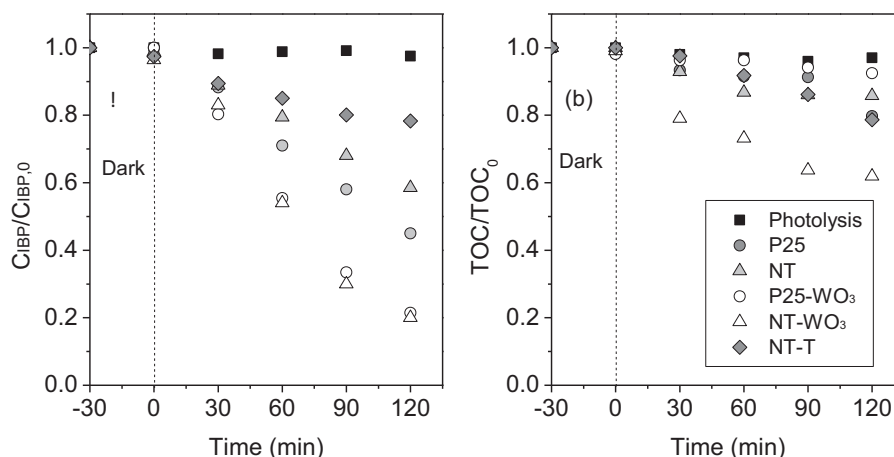

Fig. 8. Time evolution of IBP dimensionless concentration (a) and dimensionless TOC (b) during photocatalytic oxidation under visible light radiation (λ = 390–800 nm).
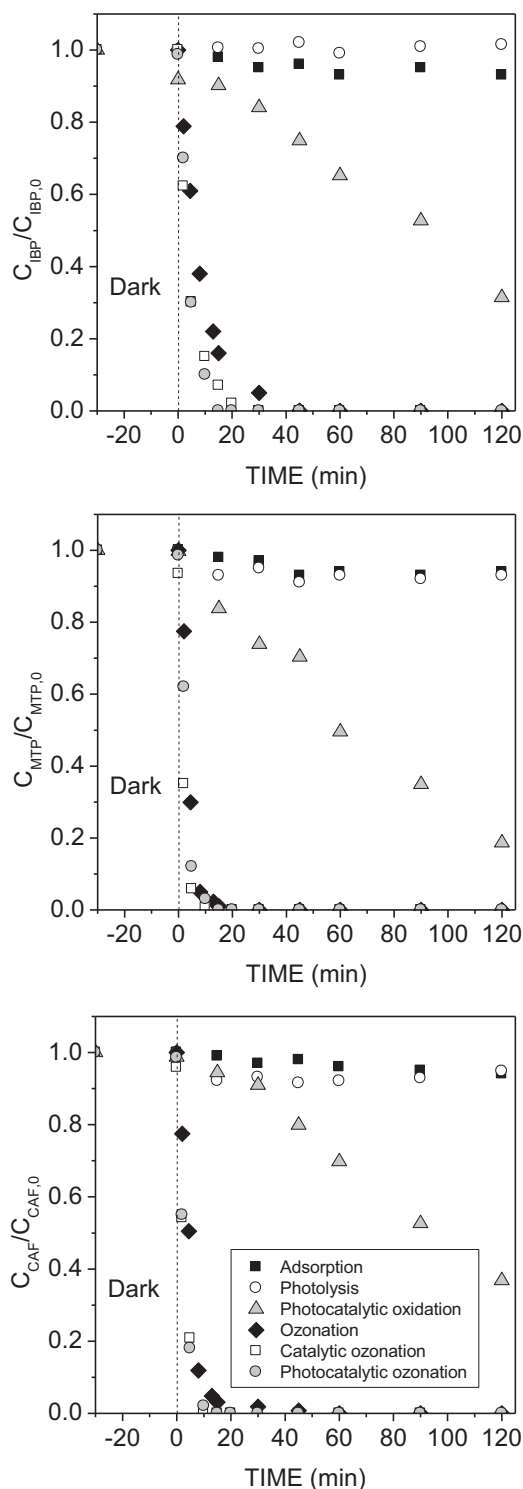
Fig. 9. Time evolution of ECs dimensionless concentration during all the treatments applied with aqueous matrix MWW effluent under simulated solar light radiation ($\lambda = 320$–800 nm) and NT–WO$_3$ catalyst.
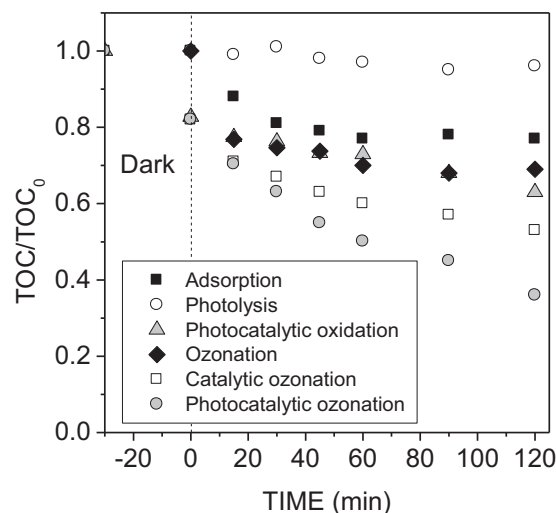

Fig. 10. Time evolution of TOC dimensionless concentration during all the treatments applied with aqueous matrix MWW effluent under simulated solar light radiation ($\lambda = 320$–800 nm) and NT–WO$_3$ catalyst.

Nishimoto et al. observed a higher TOC removal during phenol ozonation with WO$_3$ suggesting that it functions as an ozonation catalyst in a similar manner to MnO$_2$ or TiO$_2$ [38]. In addition, WO$_3$ has been widely used as the active component of O$_3$ gas sensors, in which O$_3$ undergoes dissociative adsorption onto the WO$_3$ surface [39,40]. On the other hand, another plausible explanation of the catalytic activity of TiO$_2$–WO$_3$ catalysts during ozonation compared to bare TiO$_2$ is the enhanced adsorption capacity due to the presence of WO$_3$ [18,13]. Thus, TiO$_2$ has been widely used as catalyst for ozonation processes and proposed mechanisms involve surface reactions between adsorbed O$_3$ and organic compounds [41]. The fact that bare TiO$_2$ samples studied here do not show any catalytic activity in the process could be related to an inefficient decomposition of O$_3$ due to the lack of organic matter near the catalyst surface. However, the enhanced adsorption capacity of TiO$_2$–WO$_3$ catalysts can lead to an increase in the local concentration of organic matter in the vicinity of their surface [18], thus allowing surface reactions between adsorbed O$_3$ and organic compounds. Both hypotheses should be considered but some additional work to clarify the prevailing mechanism is needed. Finally, the highest mineralization degree was obtained with the photocatalytic ozonation process regardless of the catalyst used. This is in agreement with the expected synergistic effect between ozone and irradiated semiconductors. This synergistic effect is due to the reaction of O$_3$ with conduction band electrons of TiO$_2$ and WO$_3$, or with the superoxide ion radical generated (O$_2$$^{\bullet-}$), in both cases leading to the formation of higher concentrations of hydroxyl radicals (HO$^{\bullet}$), main responsible of mineralization [5,8,38].

On the other hand, MWW parameters after the most representative treatments with NT–WO$_3$ catalyst are summarized in Table 2. As commented above, photocatalytic ozonation gave place to higher TOC depletion than individual treatments. Similar trends are observed both for COD and aromaticity, reaching a 66% COD reduction in the combined treatment compared with 10% in photocatalytic oxidation and 19% upon single ozonation. Also the effectiveness of catalytic ozonation can be observed in terms of TOC, COD and aromaticity. In addition, it can be noticed that the pH remain unalterable after the treatments applied as a consequence of the buffer effect of the IC content (from carbonate/bicarbonate) also unalterable upon the treatments.

The comparison of the catalysts in the photocatalytic ozonation process is shown with more detail in Figs. 11 and 12 which depict ECs concentration and TOC with time, respectively. Again it can be
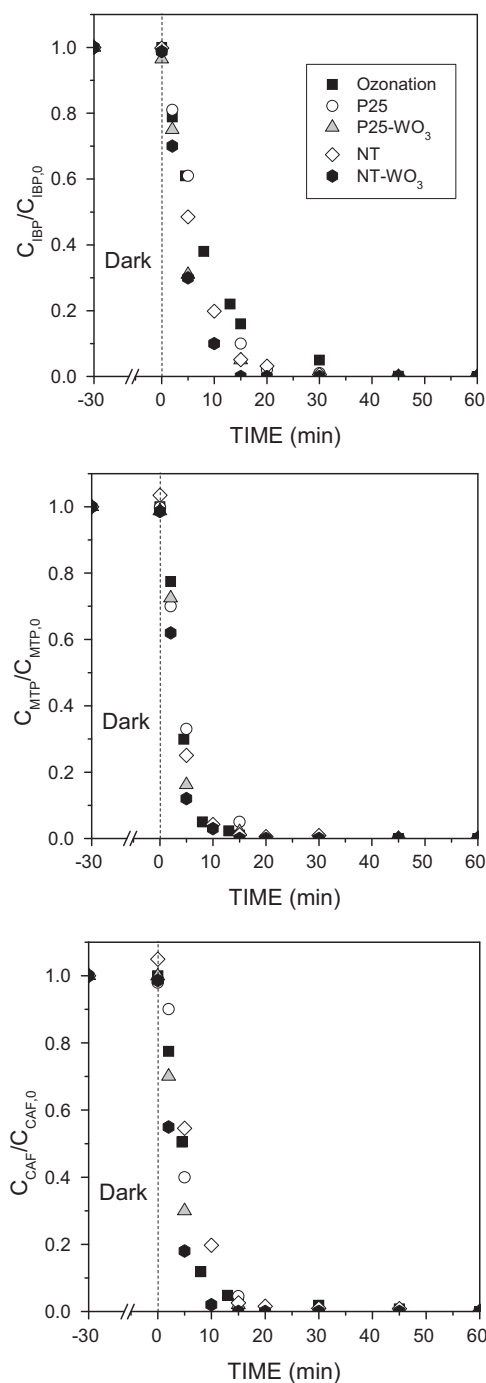
containing photocatalysts, P25–WO$_3$ and NT–WO$_3$, led to higher mineralization around 47%, with also higher TOC removal rate than ozone alone (see Fig. 10 for NT–WO$_3$), thus indicating a catalytic effect to some extent. This improvement can be related to (1) the catalytic effect of WO$_3$ and/or (2) the higher adsorption capacity of TiO$_2$–WO$_3$ catalysts. The catalytic activity of WO$_3$ in aqueous ozone decomposition or catalytic ozonation has not been extensively reported, however some evidences have been found.
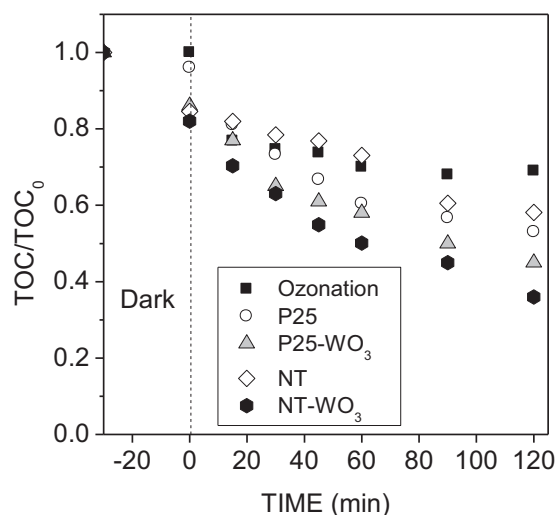
Fig. 12. Time evolution of TOC dimensionless concentration during ozonation and photocatalytic ozonation with MWW effluent as aqueous matrix under simulated solar light radiation ($\lambda = 320$–$800\,nm$) and all the catalysts studied.

in Section 3.2, but also a significant contribution of dark catalytic ozone reactions. The best performance was attained with NT–WO_3 photocatalyst which leads to 64% TOC removal. The improvement observed in the NT series after introducing the WO_3 is remarkably higher than in the P25 series in good agreement with visible light response results probably due to a better dispersion of WO_3. To elucidate the reaction mechanism of photocatalytic ozonation using NT–WO_3 catalyst it is necessary to consider the different processes involved and will be the subject of future work.

4. Conclusions

TiO_2–WO_3 composite catalysts have been synthesized with around 4% of WO_3 and visible light response, and successfully applied for the removal of emerging contaminants in urban wastewater and mineralization of the effluent through photocatalytic ozonation. Ozone alone is able to completely remove the emerging contaminants in the wastewater matrix but the mineralization degree reached is relatively low. Photocatalytic ozonation gives place to the highest mineralization rate regardless of the catalyst used. Titanate nanotubes structure is not efficient in the photocatalytic oxidation and photocatalytic ozonation processes, but it is a good precursor of composite catalysts due to its textural and surface properties. Titanate nanotubes gave place to a composite catalyst NT–WO_3 with elongated anatase particles, a well-developed porous structure and high dispersion of WO_X species showing visible light absorption capacity. The best performance of the NT–WO_3 catalyst compared to bare TiO_2 is related to several mixed contributions such as use of a greater fraction of solar light radiation, higher organic compounds adsorption capacity and catalytic activity in ozone reactions. The contribution of the different phenomena to elucidate the reaction mechanism with this catalyst will be the subject of future work.

Fig. 11. Time evolution of ECs dimensionless concentration during ozonation and photocatalytic ozonation with aqueous matrix MWW effluent under simulated solar light radiation ($\lambda = 320$–$800\,nm$) and all the catalysts studied.

noticed that ozone alone is able to completely remove the ECs in a short time. Main differences between ozonation and photocatalytic ozonation were only observed in IBP and CAF depletion according to their lower rate constant of the direct ozone reaction. In these cases, indirect and photocatalytic contributions are more important than for MTP. It can be also noticed the highest catalytic activity of WO_3 composite materials compared to TiO_2 precursors although main differences were observed in TOC evolution (Fig. 12). In addition to the differences in the adsorption capacity, the highest mineralization rate was observed for the TiO_2–WO_3 catalysts. These catalysts take the advantage of using a greater fraction of solar light radiation in the visible region due to the presence of WO_3 as demonstrated

References

[1] J.L. Santos, I. Aparicio, M. Callejón, E. Alonso, J. Hazard. Mater. 164 (2009) 1509–1516.

[2] D. Barceló, M. Petrovic (Eds.), Emerging Contaminants from Industrial and Municipal Wastes: Occurrence, Analysis and Effects, The Handbook of Environmental Chemistry 5-S1, Springer, Berlin, 2008.

[3] B. Halling-Sorensen, S. Nors-Nielsen, P.F. Lanzky, F. Ingerslev, H.C. Holten Lützhoft, S.E. Jorgensen, Chemosphere 36 (1998) 357–393.

[4] S. Esplugas, D.M. Bila, L.G.T. Krause, M. Dezotti, J. Hazard. Mater. 149 (2007) 631–642.

[5] T.E. Agustina, H.M. Ang, V.K. Vareek, J. Photochem. Photobiol., C 6 (2005) 264–273.

[6] E.M. Rodríguez, G. Fernández, P.M. Alvarez, F.J. Beltrán, Water Res. 46 (2012) 152–166.

[7] F.J. Rivas, F.J. Beltrán, A. Encinas, J. Environ. Manage. 100 (2012) 10–15.

[8] E. Mena, A. Rey, B. Acedo, F.J. Beltrán, S. Malato, Chem. Eng. J. 204–206 (2012) 131–140.

[9] M.D. Hernández-Alonso, J.M. Coronado, A.J. Maira, J. Soria, V. Loddo, V. Augugliaro, Appl. Catal., B 39 (2002) 257–267.

[10] S. Malato, P. Fernández-Ibáñez, M.I. Maldonado, J. Blanco, W. Gernjak, Catal. Today 147 (2009) 1–59.

[11] M.D. Hernández-Alonso, F. Fresno, S. Suárez, J.M. Coronado, Energy Environ. Sci. 2 (2009) 1231–1257.

[12] C. Shifu, C. Lei, G. Shen, C. Gengyu, Powder Technol. 160 (2005) 198–202.

[13] Y.T. Kwon, K.Y. Song, W.I. Lee, G.J. Choi, Y.R. Do, J. Catal. 191 (2000) 192–199.

[14] B. Tryba, M. Piszcz, A.W. Morawski, Int. J. Photoenergy (2009) 1–7 (Article ID 297319).

[15] M. Ismail, L. Bousselmi, O. Zahraa, J. Photochem. Photobiol., A 222 (2011) 314–322.

[16] M. Xiao, L. Wang, X. Huang, Y. Wu, Z. Dang, J. Alloys Compd. 470 (2009) 486–491.

[17] V. Iliev, D. Tomova, S. Rakovsky, A. Eliyas, G. Li Puma, J. Mol. Catal. A: Chem. 327 (2010) 51–57.

[18] D. Tomova, V. Iliev, S. Rakowsky, M. Anachkov, A. Eliyas, G. Li Puma, J. Photochem. Photobiol., A 231 (2012) 1–8.

[19] M.D. Hernández-Alonso, S. García-Rodríguez, B. Sánchez, J.M. Coronado, Nanoscale 3 (2011) 2233–2240.

[20] M.D. Hernández-Alonso, S. García-Rodríguez, S. Suárez, R. Portela, B. Sánchez, J.M. Coronado, Appl. Catal., B 110 (2011) 251–259.

[21] H. Bader, J. Hoigné, Water Res. 15 (1981) 449–456.

[22] K.S.W. Sing, D.H. Everett, R.A.W. Haul, L. Moscou, R.A. Pierotti, J. Rouquerol, T. Siemieniewska, Pure Appl. Chem. 57 (1985) 603–619.

[23] J. Yan, G. Wu, N. Guan, L. Li, Z. Li, X. Cao, Phys. Chem. Chem. Phys. 15 (2013) 10978–10988.

[24] I.M. Arabatzis, S. Antonaraki, T. Stergiopoulos, A. Hiskia, E. Papaconstantinou, M.C. Bernard, P. Falaras, J. Photochem. Photobiol., A 149 (2002) 237–245.

[25] M.A. Vuurman, I.E. Wachs, A.M. Hirt, J. Phys. Chem. 95 (1991) 9928–9937.

[26] C. Sanato, M. Odziemkowski, M. Ulmann, J. Augustynski, J. Am. Chem. Soc. 123 (2001) 10639–10649.

[27] K.K. Akurati, A. Vital, J.P. Dellemann, K. Michalow, T. Graule, D. Ferri, A. Baiker, Appl. Catal., B 79 (2008) 53–62.

[28] C.D. Wagner, L.E. Davis, M.V. Zeller, J.A. Taylor, R.H. Raymond, L.H. Gale, Surf. Interface Anal. 3 (1981) 211–225.

[29] M.W. Xiao, L. Wang, X.J. Huang, Y.D. Wu, Z. Dang, J. Alloys Compd. 470 (2009) 486–491.

[30] Y. Li, L. Chen, Y. Guo, X. Sun, Y. Wei, Chem. Eng. J. 181–182 (2012) 734–739.

[31] C.C. Ryan, D.T. Tan, W.A. Arnold, Water Res. 45 (2011) 1280–1286.

[32] L.E. Jacobs, L.K. Weavers, E.F. Houtz, Y.P. Chin, Chemosphere 86 (2012) 124–129.

[33] M.M. Huber, S. Canonica, G.Y. Park, U. Von Gunten, Environ. Sci. Technol. 37 (2003) 1016–1024.

[34] R. Broséus, S. Vincent, K. Aboulfadl, A. Daneshvar, S. Sauvé, B. Barbeau, M. Prévost, Water Res. 43 (2009) 4707–4717.

[35] I. Sires, N. Oturan, M.A. Oturan, Water Res. 44 (2010) 3109–3120.

[36] M.M. Huber, A. Gobel, A. Joss, N. Hermann, D. Loffler, C. McArdell, A. Ried, H. Siegrist, T.A. Ternes, U. Von Gunten, Environ. Sci. Technol. 39 (2005) 4290–4299.

[37] F.J. Benítez, J.L. Acero, F.J. Real, G. Roldán, Chemosphere 77 (2009) 53–59.

[38] S. Nishimoto, T. Mano, Y. Kameshima, M. Miyake, Chem. Phys. Lett. 500 (2010) 86–89.

[39] J. Guerin, K. Aguir, M. Bendahan, Sens. Actuators, B 119 (2006) 327–334.

[40] V. Oison, L. Saadi, C. Lambert-Mauriat, R. Hayn, Sens. Actuators, B 160 (2011) 505–510.

[41] B. Kasprzyk-Hordern, M. Ziólek, J. Nawrocki, Appl. Catal., B 46 (2003) 639–669.